symmetry

MDPI

Article

Foldable/Deployable Spherical Mechanisms Based on Regular Polygons

Raffaele Di Gregorio

Laboratory of Mechatronics and Virtual Prototyping (LaMaViP), Department of Engineering, University of Ferrara, Via Saragat 1, 44122 Ferrara, Italy; raffaele.digregorio@unife.it; Tel.: +39-0532-974828

Abstract

The possibility of satisfying special geometric conditions, either through their architecture or through their configuration, makes a mechanism acquire changeable motion characteristics (kinematotropic or metamorphic behavior, multi-mode operation capability, etc.) that are of interest. Aligning revolute (R)-pair axes is one of such special conditions. In spherical linkages, only R-pairs, whose axes share a common intersection (spherical motion center (SMC)), are present. Investigating how R-pair axes can become collinear in a spherical mechanism leads to the identification of those that exhibit changeable motion features. This approach is adopted here to select non-redundant spherical mechanisms coming from regular polygons that are foldable/deployable and have a wide enough workspace for performing motion tasks. This analysis shows that the ones with hexagonal architecture prevail over the others. These results are exploitable in many contexts related to field robotics (aerospace, machines for construction sites, deployable antennas, etc.)

Keywords: singularity; origami; reconfigurable mechanism; kinematotropic mechanism; metamorphic mechanism

Academic Editors: Christian Iandiorio and Fabio Botta

Received: 5 July 2025
Revised: 30 July 2025
Accepted: 1 August 2025
Published: 9 August 2025

Citation: Di Gregorio, R. Foldable/Deployable Spherical Mechanisms Based on Regular Polygons. *Symmetry* **2025**, *17*, 1281. https://doi.org/10.3390/sym17081281

1. Introduction

Mechanisms with a foldable/deployable capability are a subset of *reconfigurable* mechanisms [1], which are mainly categorized into *kinematotropic* mechanisms [2–9], *metamorphic* mechanisms [10–16], and *multiple-operation-mode* mechanisms [17–20]. Kinematotropic mechanisms [2] are mechanisms that, without changing their topology, may change their finite mobility (i.e., their degrees-of-freedom (DOFs)) by passing through a transition configuration, which is a bifurcation or a multi-furcation configuration, shared by different branches of motions they can work in. In contrast, metamorphic mechanisms [1] are mechanisms that can change their finite mobility or their link connectivity with a topology change at transition configurations where link annexation and/or changes of joint properties occur. Eventually, multiple-operation mode mechanisms [19] are mechanisms that, without changing mobility and topology, may change their motion pattern (operation mode) at transition configurations named *constraint singularities* [17]. Collinearity of revolute (R) pairs' axes [3,4,6,8,9] is one of the geometric conditions used to generate reconfigurable mechanisms.

Investigating whether the deduction of foldable/deployable spherical mechanisms from regular polygons leads to mechanisms of practical interest is the aim of this work. Spherical linkages (SLs) contain only R-pairs with axes that share a common intersection point, named the *spherical motion center* (SMC). Therefore, a deployable SL, when deployed, disposes the R-pair axes on a plane, as rays radiating from one point; furthermore, on the same plane, the connection between couples of R-pair axes, due to the links, appears as segments joining these axes. This observation leads to the conclusion that the resulting planar image of the deployed SL is always a piecewise linear curve whose vertices lie on lines that converge toward the SMC, while the single-loop SLs always generate planar polygons when deployed.

Starting with this conclusion, this work studies the foldable/deployable single-loop SLs whose planar images are regular polygons. In particular, investigating how R-pair axes can become collinear in these SLs will lead to a selection of those that exhibit changeable motion features. Then, specific kinematic analyses on the selected SLs will highlight which ones have a workspace wide enough for performing motion tasks of practical interest.

The results of this study are of interest in many fields. For instance, field robotics encompass applications where machines must be mounted on site and frequently moved from one place to another. Additionally, sometimes (e.g., in aerospace applications and, in general, in hazardous environments) these operations cannot be managed directly by on-site workers. In this context, transportation requires minimizing the transported volume. Therefore, machine architectures that can be folded for their transportation, and autonomously deployed on site for their operation, would be appealing. Moreover, foldable/deployable capability is of interest in packaging, where different shapes of boxes are generated from one sheet, or in MEMS/NEMS, where the miniaturized machines are manufactured by starting with a single layer of suitable material. Furthermore, foldability/deployability is the central skill of *origami* [21,22], which is the old Japanese art of generating paper mechanisms or structures by suitably folding one paper sheet. Origami's artefacts share with spherical linkages the presence of only R-pairs as joints, since each crease of these artefacts is indeed an R-pair. Foldable/deployable linkages with only R-pairs have been studied in a number of papers (see, for instance, [7,22–24]).

The paper is structured as follows: Section 2 gives the necessary background materials, analyzes the deployable SLs obtainable from regular polygons, and selects the most promising ones. Section 3 presents the kinematic analyses of the SLs selected in the previous section. Then, Section 4 discusses the results and Section 5 draws the conclusions.

2. Materials and Methods

Regular polygons are, by definition, closed, planar shapes with all sides equal in length (congruent sides), and with all interior angles equal in measure (congruent interior angles). They can be convex (e.g., equilateral triangle, square, regular pentagon, etc. (Figure 1a)) or star-shaped (i.e., non-convex star-shaped figures (Figure 1b)). Only convex regular polygons (CRPs) are of interest for generating foldable/deployable SLs.

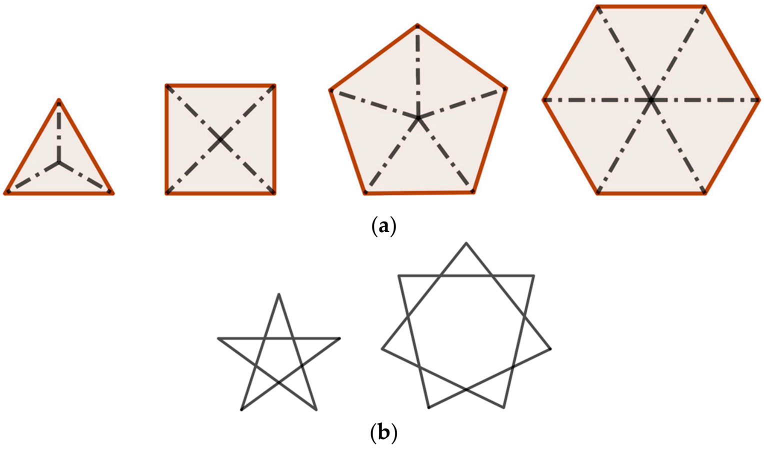
(**a**)

(**b**)

Figure 1. Examples of regular polygons: (**a**) convex and (**b**) star-shaped.

The drawing of a CRP with n sides is transformable into the deployed kinematic scheme of a possible SL with n links and n R-pairs by associating, to each CRP side, one link and, to each CRP vertex, one R-pair with an axis that passes through the vertex itself and the center of the CRP (see Figure 2). If the finite mobility of the so-generated SLs is computed through the Chebychev–Grübler–Kutzbach criterion [25] (i.e., by taking into account only the number of links and the number and types of joints), they have a non-negative mobility, l, when considered as spherical mechanisms, which is given by the following formula:

$$l = 3(n-1) - 2n = n - 3, \tag{1}$$

but, for n up to 6, they are overconstrained when considered as spatial mechanisms (it is worth reminding that the Chebychev–Grübler–Kutzbach criterion [25] becomes $l = 6(n-1) - 5n = n - 6$ for a spatial mechanism with n links and n R-pairs). This means that, if geometric errors that make the R-pair axes do not share a common intersection point any longer are present, mechanism jamming occurs when $n \leq 6$.

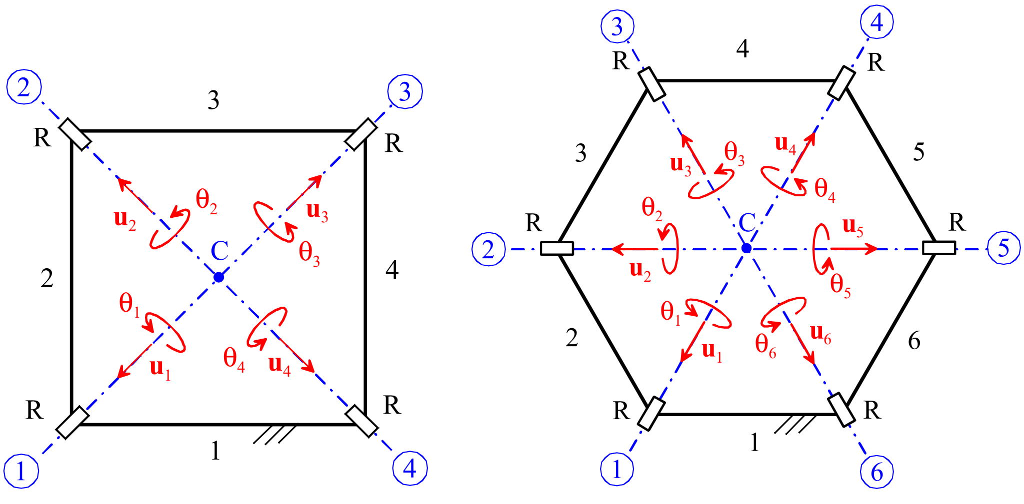

(**a**) (**b**)

Figure 2. Kinematic schemes of deployed SLs generated from a square (**a**) and a regular hexagon (**b**) (R stands for R-pair; point C is the SMC and the center of the regular polygon; the black numbers are the link numbers; the circled blue numbers are the joint numbers and, at the same time, the vertex numbers).

Equation (1) reveals that a positive mobility (i.e., a real SL) is obtainable for n greater than 3, and that with n = 6, the SL has 3 DOF; thus, it is able to make the output link perform a general spherical motion inside its workspace, whereas it is a redundant SL for n greater than 6. Additionally, there are collinear R-pairs only when all of the diagonals of the CRP pass through the center of the CRP, that is, only when n is even. Collinearity of R-pair couples is a necessary condition to obtain a foldable linkage. All of these observations lead to the conclusion that non-redundant foldable/deployable SLs are obtainable only from squares (n = 4) or regular hexagons (n = 6). Below, in this section, the foldability/deployability of these two SL architectures will be analyzed.

The instantaneous (elementary) mobility of the so-generated SLs is computable by applying the relative motion theorems [26] to the single-loop kinematic chain of the generic SL generated from the CRP with n sides as follows:

$$\left.\begin{array}{l}\boldsymbol{\omega}_{(i+1)i}=\dot{\theta}_i\mathbf{u}_i,\ for\ i=1,\ldots,n-1\\ \boldsymbol{\omega}_{1n}=\dot{\theta}_n\mathbf{u}_n\\ \mathbf{0}=\boldsymbol{\omega}_{11}=\boldsymbol{\omega}_{1n}+\sum\limits_{i=1,n-1}\boldsymbol{\omega}_{(i+1)i}\end{array}\right\}\Rightarrow\mathbf{0}=\sum_{i=1,n}\dot{\theta}_i\mathbf{u}_i \quad (2)$$

where

- $\boldsymbol{\omega}_{jk}$ denotes the angular velocity of link j when measured from link k,
- $\mathbf{u}_i$ is the unit vector of the axis of the i-th R-pair with direction from the CRP center to the i-th vertex of the CRP (see Figure 2), and
- the angle θ_i is the joint variable of the i-th R-pair (see Figure 2), which is positive if counterclockwise with respect to $\mathbf{u}_i$, and equal to zero when the two links joined by the i-th R-pair are fully folded on one another.

Equation (2) is a vector equation that corresponds to a system of three scalar equations, which are linear and homogeneous in the n joint rates $\dot{\theta}_i$, for $i = 1, \ldots, n$; as a consequence, the local mobility is equal to n minus the rank of system (2). The rank of this system depends on the mechanism configuration. The configurations where it is equal to three (i.e., full rank) are the ordinary non-singular configurations, which are geometrically identifiable by the fact that the R-pair axes are not coplanar (i.e., where the set of unit vectors $\{\mathbf{u}_i \mid i = 1, \ldots, n\}$ spans a 3-dimensional vector space), and the local mobility coincides with the finite mobility given by Equation (1). Conversely, when the R-pair axes are coplanar, as it happens at a fully-deployed or folded configuration, the local mobility increases by one unit and it is higher than the finite mobility, which makes a singular configuration named *uncertainty configuration* [27] occur. This transitory extra mobility is exploitable to make the SL switch from one operation mode to another; thus, these uncertainty configurations become the transition configurations of the studied SLs.

2.1. Foldability/Deployability of SLs Generated from Squares (Square SLs)

Square SLs (Figure 2a) have one DOF at non-singular configurations (Equation (1) with $n = 4$), but at deployed/folded configurations (Equation (2) with $n = 4$ and coplanar axes of the R-pairs), they acquire one further local DOF; that is, they have two local DOFs.

The analysis of these SL architectures reveals that they have four operation modes (see Figure 3) and four transition (uncertainty) configurations (Figures 2a and 4). In particular, their operation modes are the following four:

(i) semi-deployed mode with rotation around the axis of joint 1 (Figure 3a), in which joints 2 and 4 are locked, whereas joint 3 is constrained to satisfy the relationship $\theta_3 = -\theta_1$;
(ii) semi-deployed mode with rotation around the axis of joint 4 (Figure 3b), in which joints 1 and 3 are locked, whereas joint 2 is constrained to satisfy the relationship $\theta_2 = -\theta_4$;
(iii) semi-folded mode with rotation around the axis of joint 1 (Figure 3c), in which joints 2 and 4 are locked, whereas joint 3 is constrained to satisfy the relationship $\theta_3 = \theta_1$;
(iv) semi-folded mode with rotation around the axis of joint 4 (Figure 3d), in which joints 1 and 3 are locked, whereas joint 2 is constrained to satisfy the relationship $\theta_2 = \theta_4$.

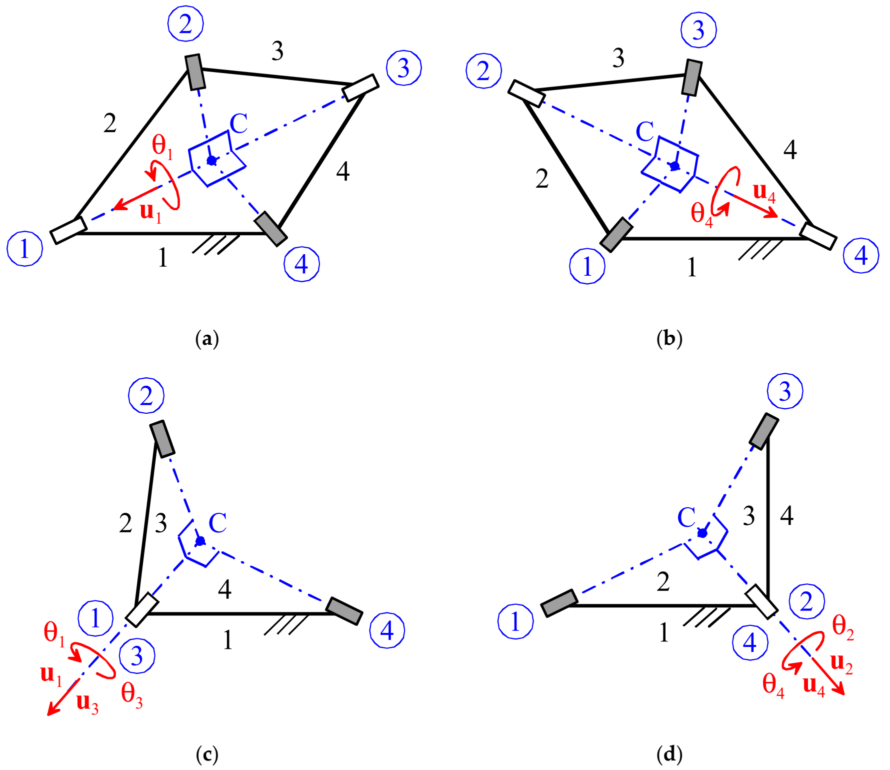

(**a**) (**b**)

(**c**) (**d**)

Figure 3. Operation modes of a square SL (the gray rectangles indicate the locked joints): (**a**) 1st semi-deployed mode, (**b**) 2nd semi-deployed mode, (**c**) 1st semi-folded mode, and (**d**) 2nd semi-folded mode.

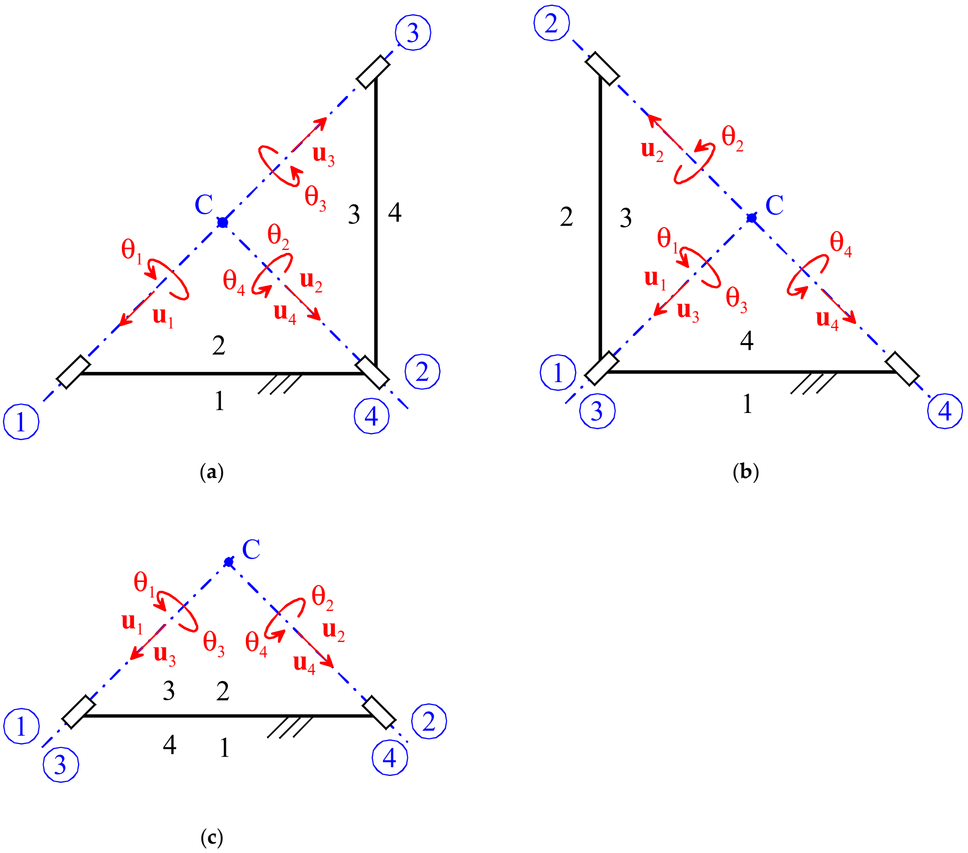

(**a**) (**b**)

(**c**)

Figure 4. Folded configurations of a square SL: (**a**) 1st semi-folded configuration, (**b**) 2nd semi-folded configuration, and (**c**) fully-folded configuration.

Their transition configurations are the following four:

(a) fully-deployed configuration (Figure 2a);
(b) 1st semi-folded configuration (Figure 4a), whose folded edge coincides with the axis of joint 1;
(c) 2nd semi-folded configuration (Figure 4b), whose folded edge coincides with the axis of joint 4; and
(d) fully-folded configuration (Figure 4c).

How to devise the hardware to allow the overlapping of links and/or joints without collisions or interferences at the folded/semi-folded configurations (Figure 4) will be discussed later, in Section 3.

The relationships among transition configurations and operation modes are expressible through a graph (transition graph) whose nodes are associated with the operation modes and whose edges are associated with the transition configurations. Figure 5 shows the transition graph of a square SL. In Figure 5, i, ii, iii, and iv refer to the above-defined operation modes shown in Figure 3a, Figure 3b, Figure 3c, and Figure 3d, respectively; whereas a, b, c, and d refer to the above-defined transition configurations shown in Figure 2a, Figure 4a, Figure 4b, and Figure 4c, respectively. The possibility of drawing a transition graph highlights that, if all of the operation modes must be exploited, the motion control of such SLs must use techniques applicable to *finite-state machines* [28], where the states are the operation modes, with specific actions to implement at the transition configurations for making the SL move into the desired operation mode.

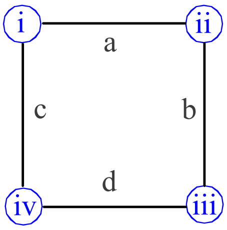

Figure 5. Transition graph of a square SL (i, ii, iii, and iv refer to the operation modes shown in Figure 3a, Figure 3b, Figure 3c, and Figure 3d, respectively; whereas a, b, c, and d refer to the transition configurations shown in Figure 2a, Figure 4a, Figure 4b, and Figure 4c, respectively).

2.2. Foldability/Deployability of SLs Generated from Hexagons (Hexagonal SLs)

Hexagonal SLs (Figure 2b) have 3 DOFs at non-singular configurations (Equation (1) with $n = 6$); however, at deployed/folded configurations (Equation (2) with $n = 6$ and coplanar axes of the R-pairs), they acquire one further local DOF, that is, they have 4 local DOFs.

The analysis of these SL architectures reveals that they have 4 operation modes (see Figure 6) and 5 transition (uncertainty) configurations (Figures 2b and 7). In particular, their operation modes are the following four:

(i) parallel-wrist mode (Figure 6a), in which the SL has three DOFs, that is, three joint variables are computable as functions of the other three (e.g., θ_2, θ_3, and θ_4 as functions of θ_1, θ_6, and θ_5) by solving a suitable constraint equation system;
(ii) flapping-wings mode (Figure 6b), in which joints 2 and 5 are locked, joints 3 and 4 are constrained to satisfy the relationships $\theta_1 = \theta_3$ and $\theta_6 = \theta_4$, respectively, and the SL has two DOFs;
(iii) left serial mode (Figure 6c), in which joints 3 and 6 are locked, joints 4 and 5 are constrained to satisfy the relationships $\theta_1 = \theta_5$ and $\theta_2 = \theta_4$, respectively, and the SL has two DOFs;

(iv) right serial mode (Figure 6d), in which joints 1 and 4 are locked, joints 2 and 3 are constrained to satisfy the relationships $\theta_6 = \theta_2$ and $\theta_5 = \theta_3$, respectively, and the SL has two DOFs.

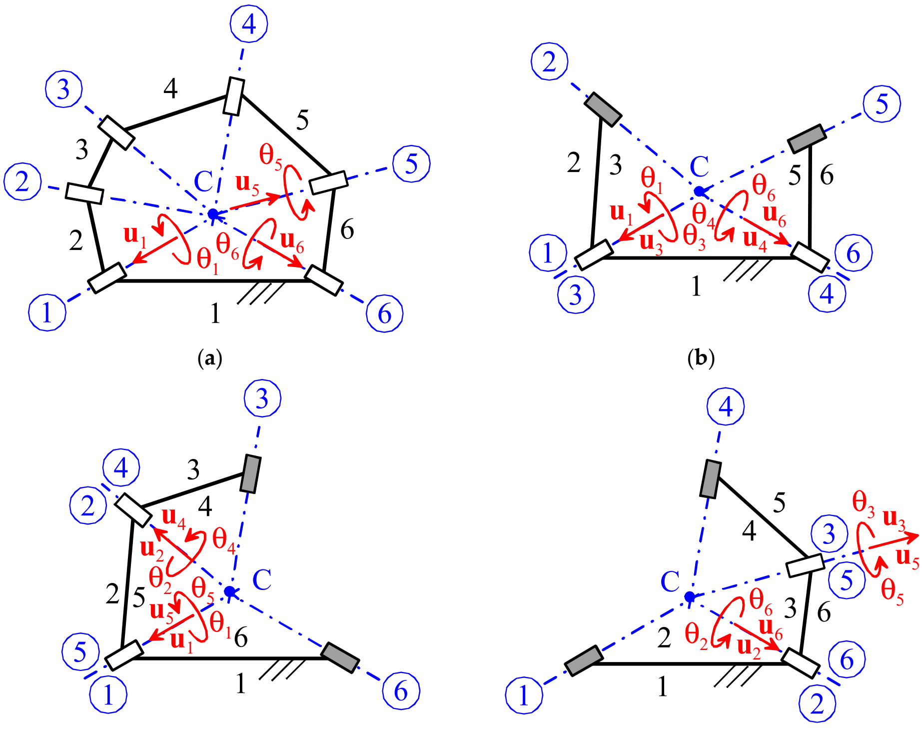

(**a**) (**b**)

(**c**) (**d**)

Figure 6. Operation modes of a hexagonal SL (the gray rectangles indicate the locked joints): (**a**) parallel-wrist mode, (**b**) flapping-wing mode, (**c**) left serial mode, and (**d**) right serial mode.

Their transition configurations are the following five:

(a) fully-deployed configuration (Figure 2b),

(b) 1st (symmetric) semi-folded configuration (Figure 7a) whose folded edge coincides with the collinear axes of joints 2 and 5,

(c) 2nd (left) semi-folded configuration (Figure 7c) whose folded edge coincides with the collinear axes of joints 3 and 6,

(d) 3rd (right) semi-folded configuration (Figure 7d) whose folded edge coincides with the collinear axes of joints 1 and 4, and

(e) fully-folded configuration (Figure 7b).

Figure 8 shows the transition graph of a hexagonal SL. In Figure 8, i, ii, iii, and iv refer to the above-defined operation modes shown in Figure 6a, Figure 6b, Figure 6c, and Figure 6d, respectively, whereas a, b, c, d, and e refer to the above-defined transition configurations shown in Figure 2b, Figure 7a, Figure 7c, Figure 7d, and Figure 7b, respectively. The fully-deployed configuration (Figure 2b) is a transition configuration between *assembly modes*, which are the multiple solutions of the constraint equation system, of the parallel-wrist mode (Figure 6a). Furthermore, the exploitation of the fully-folded mode (Figure 7b) as a direct transition configuration between 2-DOF operation modes is difficult in practice due to link/joint collisions that are difficult to eliminate by using suitable link/joint geometries. Even though the direct transition between these modes is usually forbidden by the machine hardware, indirect transitions are possible by passing through the parallel-wrist mode (Figure 6a), as the transition graph (Figure 8) shows, by using suitable geometries of the links.

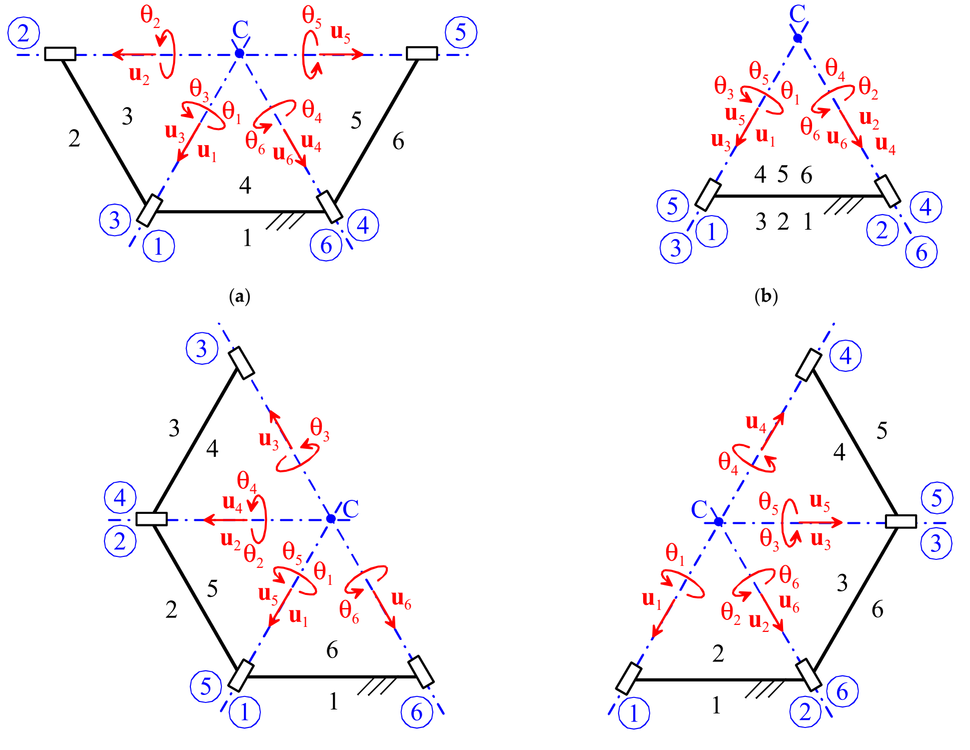

Figure 7. Folded configurations of a hexagonal SL: (**a**) 1st (symmetric) semi-folded configuration, (**b**) fully-folded configuration, (**c**) 2nd (left) semi-folded configuration, and (**d**) 3rd (right) semi-folded configuration.

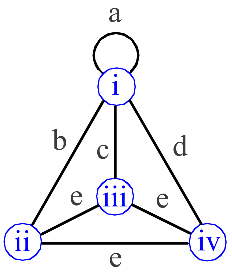

Figure 8. Transition graph of a hexagonal SL (i, ii, iii, and iv refer to the operation modes shown in Figure 6a, Figure 6b, Figure 6c, and Figure 6d, respectively; whereas a, b, c, d and e refer to the transition configurations shown in Figure 2b, Figure 7a, Figure 7c, Figure 7d, and Figure 7b, respectively).

3. Results

The previous section has identified square and hexagonal SLs as possible foldable/deployable SLs. This section deals with kinematics and workspaces of the operation modes of these SLs.

3.1. Square SLs

All of the four operation modes of square SLs (Figure 3) make them behave as an R-pair, which can perform either a complete rotation, if the link-interference problems are somehow solved (see below), or a quasi-complete rotation, if those problems are not solved. With respect to a simple R-pair, square SLs have the peculiarity of being able to switch the direction of the R-pair axis between two mutually orthogonal directions.

In particular, the switching between modes (i) (Figure 3a) and (ii) (Figure 3b) is always possible, since it is obtainable by passing through the fully-deployed configuration

(Figure 2a), which has no overlapping of links and/or joints. On the other hand, obtaining modes (iii) (Figure 3c) and (iv) (Figure 3d) require the adoption of particular geometries of links and joints, like the ones shown in Figure 9, to avoid interferences among them. The geometry of Figure 9a is compatible with operation modes (i) (Figure 3a), (ii) (Figure 3b), and (iii) (Figure 3c), and, in operation mode (ii), it allows for a complete rotation; whereas the geometry of Figure 9b is compatible with operation modes (i) (Figure 3a), (ii) (Figure 3b), and (iv) (Figure 3d), and, in operation mode (i), it allows for a complete rotation. Nevertheless, both of these geometries cannot assume the fully-folded configuration (Figure 4c); as a consequence, they cannot switch from one into the other.

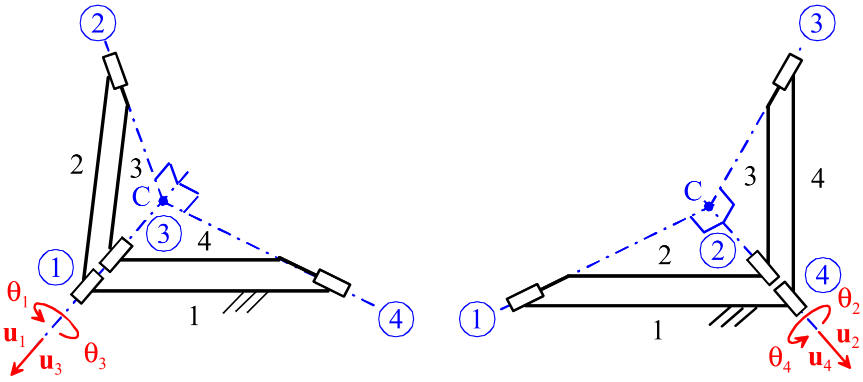

(**a**) (**b**)

Figure 9. Special geometries of square SLs: (**a**) geometry compatible with operation modes (i) (Figure 3a), (ii) (Figure 3b), and (iii) (Figure 3c), and (**b**) geometry compatible with operation modes (i) (Figure 3a), (ii) (Figure 3b), and (iv) (Figure 3d).

Other hardware arrangements are possible for avoiding interferences during the transition between particular operation modes, but devising a geometry compatible with all of the four operation modes is difficult.

3.2. Hexagonal SLs

The four operation modes of hexagonal SLs (see Figure 6) have different kinematic behaviors, as explained below.

3.2.1. Flapping-Wing Mode

The flapping-wing mode (Figure 6b) has two DOFs. In this operation mode, the mechanism behaves as a mechanical system constituted of two mobile links that are independently hinged on a frame, that is, it consists of two independent single-DOF mechanisms. Its kinematic analysis is simple. Each mobile link can perform an almost-complete rotation around the axis of the R-pair that joins it to the frame. The limitations on the rotations are due to the avoidance of link/joint inferences.

This mode is reachable (Figure 8), passing through the transition configuration (b) (symmetric semi-folded configuration (Figure 7a)), which needs particular geometries of links and joints to avoid link/joint interference. Figure 10 shows one of these particular geometries.

3.2.2. Left and Right Serial Modes

Left (Figure 6c) and right (Figure 6d) serial modes are both two-DOF operation modes. In these modes, the hexagonal SL behaves as a serial pointing system, which is a serial mechanism that is able to freely orientate a line, fixed to the distal link, inside a finite workspace.

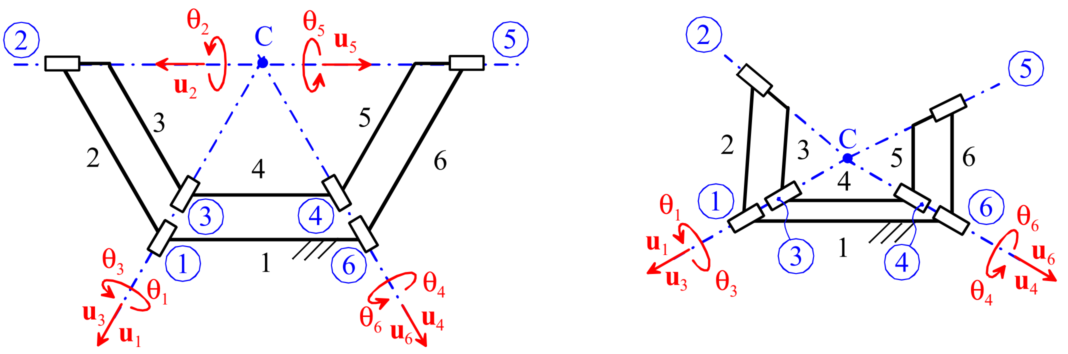

(**a**) (**b**)

Figure 10. Example of hexagonal SL geometry that can reach the symmetric semi-folded configuration (**a**) and that can operate in flapping-wing mode (**b**) without link/joint interferences.

In the left (right) serial mode, links 1 and 6 (links 1 and 2) have no relative motion and can be considered as a unique frame, hereafter named link f. Links 2 and 5 (links 3 and 6) behave as a unique intermediate link, hereafter named link e, and the same holds for links 3 and 4 (links 4 and 5), which behave as a unique distal link, hereafter named link d. Links f and e are connected through R-pairs 1 and 5 (R-pairs 6 and 2), which behave as a unique R-pair, hereafter referred to as R-pair f. Links e and d are connected through R-pairs 2 and 4 (R-pairs 3 and 5), which behave as a unique R-pair, hereafter referred to as R-pair e. Eventually, the distal R-pair 3 (R-pair 4), hereafter referred to as R-pair d, together with R-pair 6 (R-pair 1), hereafter referred to as R-pair o, are locked. The resulting simplified scheme of the left serial mode is shown in Figure 11, where $\alpha = 60°$ and the two joint variables θ_f and θ_e control the mechanism configuration.

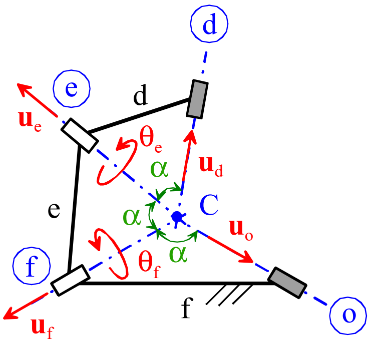

Figure 11. Simplified kinematic scheme of the left serial mode ($\alpha = 60°$; the gray rectangles indicate the locked joints).

The kinematic analyses of left and right serial modes are similar. Indeed, they are specular with respect to a plane of symmetry passing through the bisector line of the angle formed by the axes of joints 1 and 6 and perpendicular to the plane these two axes lie on. The reflection through this plane of symmetry states a one-to-one correspondence between configurations of the left serial mode and configurations of the right serial mode. Consequently, it is sufficient to analyze the kinematics of one of them. In the following part of this subsection, the left serial mode (Figures 6c and 11) will be used to illustrate the kinematics of both of these two serial modes.

With reference to Figure 11, let the axis of R-pair d be the reference line fixed to link d to use for analyzing the extension of this mode's workspace. Such a line can always perform an almost-complete rotation around the axis of joint f, whatever the angle it forms with the axis of joint f is, because the range of motion of joint variable θ_f is an almost-complete rotation. Moreover, the angle it forms with the axis of joint f can range between almost 0°, when joint variable θ_e reaches its minimum absolute value, and 2α (=120°), when θ_e is equal to 180° (i.e., when $\mathbf{u}_f$, $\mathbf{u}_e$, and $\mathbf{u}_d$ are coplanar and not overlapped). The limitations on the rotations are due to the avoidance of link/joint interferences. The so-determined workspace is wide enough for many pointing applications (see, for instance, Ref. [29]).

The direct position analysis (i.e., the computation of $\mathbf{u}_d$ for assigned values of the joint variables θ_f and θ_e) is trivial. Indeed (see Figure 11), the following relationships hold

$$\mathbf{u}_e = \mathbf{u}_f \cos\alpha + \sin\alpha\left[\sin\theta_f \frac{\mathbf{u}_f \times \mathbf{u}_o}{\sin\alpha} + \cos\theta_f \frac{(\mathbf{u}_f \times \mathbf{u}_o) \times \mathbf{u}_f}{\sin\alpha}\right] \tag{3a}$$

$$\mathbf{u}_d = \mathbf{u}_e \cos\alpha + \sin\alpha\left[\sin\theta_e \frac{\mathbf{u}_e \times \mathbf{u}_f}{\sin\alpha} + \cos\theta_e \frac{(\mathbf{u}_e \times \mathbf{u}_f) \times \mathbf{u}_e}{\sin\alpha}\right] \tag{3b}$$

which allow for the direct computation of $\mathbf{u}_d$ (i.e., of the direction of the reference line) when the joint variables θ_f and θ_e are known, since $\mathbf{u}_o$ and $\mathbf{u}_f$ are known unit vectors fixed to the frame.

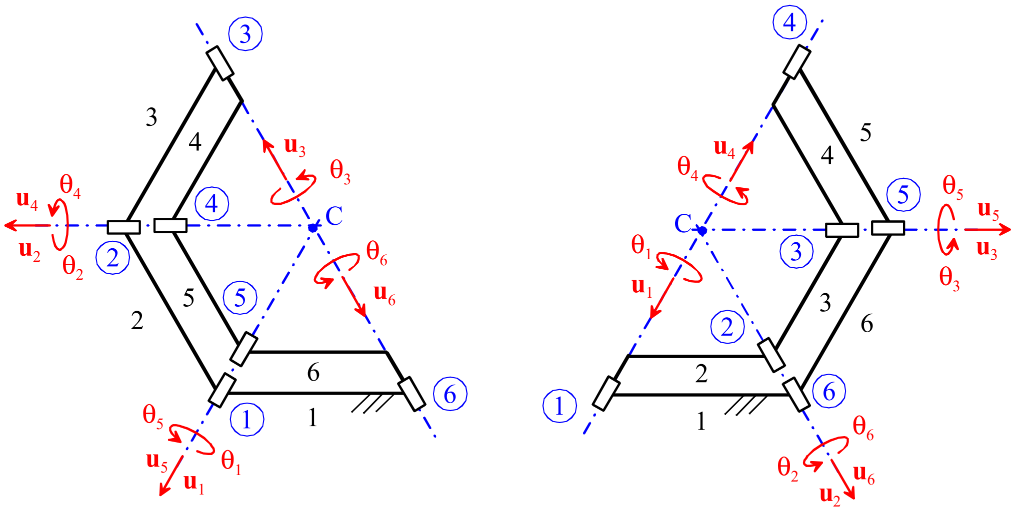

(**a**) (**b**)

Figure 12. Examples of particular hexagonal SL geometries: (**a**) geometry that can reach the left semi-folded configuration, and (**b**) geometry that can reach the right semi-folded configuration.

The inverse position analysis (i.e., the computation of joint variables θ_f and θ_e for an assigned $\mathbf{u}_d$) is easy to solve in closed form. It has up to two solutions, which geometrically (see Figure 11) correspond to the up to two intersection lines of two cones, both with point C as the apex and α as the semiangle, one with line d as the axis and the other with line f as the axis. From an analytic point of view, these solutions are obtainable by replacing Formula (3a) for $\mathbf{u}_e$ into Equation (3b), and then by algebraically manipulating the resulting equations.

The left (right) serial mode is reachable (Figure 8) by passing through the transition configuration (c), shown in Figure 7c (the transition configuration (d), shown in Figure 7d), which needs particular geometries of links and joints to avoid link/joint interference. Figure 12 shows one of these particular geometries. These geometries, while allowing the transition between the parallel-wrist mode and the left (right) serial mode, usually forbid reaching the transition configuration (e), that is, the fully-folded configuration (Figure 7b), thus forbidding the transition between all of the 2-DOF modes (Figure 8).

3.2.3. Parallel-Wrist Mode

The parallel-wrist mode (Figure 6a) is an operation mode with three DOFs. In this mode, a hexagonal SL is able to orientate one link freely with respect to the frame inside its workspace. With reference to Figure 6a, since link 1 is the frame, the only link with connectivity (reminder: connectivity [29] is the DOF number of the relative motion between two links in a mechanism) equal to three, with respect to link 1, is link 4; consequently, only link 4 is freely orientable. In general, only the links that are opposite to one another have connectivity three in a hexagonal SL.

In parallel wrists (PWs), the actuated joints are chosen on or near the frame in order to reduce the mobile masses. Accordingly, in the following part of this subsection, joints 1, 6, and 5 (Figure 6a) are chosen as actuated joints. With this choice, the actuators directly control the three joint variables, θ_1, θ_6, and θ_5, whereas the remaining three joint variables, that is, θ_2, θ_3, and θ_4, are the passive ones that are analytically/numerically relatable to the actuated ones by solving a suitable constraint equation system.

With reference to Figures 6a and 11 and to Equation (3), the following relationships hold (reminder: the angle, α, between the two joint axes fixed to the same link is always equal to 60° in a hexagonal SL):

$$\mathbf{u}_2 = \frac{1}{2}\mathbf{u}_1 + \sin\theta_1(\mathbf{u}_1 \times \mathbf{u}_6) + \cos\theta_1[(\mathbf{u}_1 \times \mathbf{u}_6) \times \mathbf{u}_1] \tag{4a}$$

$$\mathbf{u}_3 = \frac{1}{2}\mathbf{u}_2 + \sin\theta_2(\mathbf{u}_2 \times \mathbf{u}_1) + \cos\theta_2[(\mathbf{u}_2 \times \mathbf{u}_1) \times \mathbf{u}_2] \tag{4b}$$

$$\mathbf{u}_5 = \frac{1}{2}\mathbf{u}_6 + \sin\theta_6(\mathbf{u}_6 \times \mathbf{u}_1) + \cos\theta_6[(\mathbf{u}_6 \times \mathbf{u}_1) \times \mathbf{u}_6] \tag{4c}$$

$$\mathbf{u}_4 = \frac{1}{2}\mathbf{u}_5 + \sin\theta_5(\mathbf{u}_5 \times \mathbf{u}_6) + \cos\theta_5[(\mathbf{u}_5 \times \mathbf{u}_6) \times \mathbf{u}_5] \tag{4d}$$

$$\mathbf{u}_3 \cdot \mathbf{u}_4 = \frac{1}{2} \tag{4e}$$

$$\mathbf{u}_2 \cdot \mathbf{u}_3 = \frac{1}{2} \tag{4f}$$

$$\mathbf{u}_4 \cdot \mathbf{u}_5 = \frac{1}{2} \tag{4g}$$

In Equations (4a)–(4d), unit vectors $\mathbf{u}_1$ and $\mathbf{u}_6$ are known in a reference system fixed to the frame (link 1), since they are fixed to the frame, whereas unit vectors $\mathbf{u}_3$ and $\mathbf{u}_4$ are fixed to link 4 and, when known in a reference system fixed to the frame, they identify the pose of link 4 with respect to the frame. Consequently, the direct position analysis of a hexagonal SL in parallel-wrist mode is reducible to the determination of unit vectors $\mathbf{u}_3$ and $\mathbf{u}_4$, in a reference system fixed to the frame, for assigned values of the actuated joint variables θ_1, θ_6, and θ_5. Vice versa, its inverse position analysis is the determination of the values of the actuated joint variables, θ_1, θ_6, and θ_5, that are compatible with the assigned values of unit vectors $\mathbf{u}_3$ and $\mathbf{u}_4$ in a reference system fixed to the frame.

Equation (4e) allows the solution of the direct position analysis to be as follows. The known actuated joint variables θ_1, θ_6, and θ_5 make unit vectors $\mathbf{u}_2$ (Equation (4a)), $\mathbf{u}_4$ (Equation (4d)), and $\mathbf{u}_5$ (Equation (4c)) known, too, and unit vector $\mathbf{u}_3$ uniquely a function of the unknown θ_2. The introduction of these known vectors and this function into Equation (4e) makes it a trigonometric equation in θ_2, which has the following canonical form:

$$a_2 \cos\theta_2 + a_1 \sin\theta_2 + a_0 = 0 \tag{5}$$

where a_0, a_1, and a_2 are known constants that are computable through simple algebraic manipulations. Equation (5) is transformable into a quadratic equation in $t = \tan(\theta_2/2)$ through the half-angle tangent substitution, that is, the introduction of the trigonometric identities $\cos\theta_2 = (1 - t^2)/(1 + t^2)$ and $\sin\theta_2 = 2t/(1 + t^2)$; this quadratic equation is, then, solvable in closed form through the following formula:

$$t_i = \frac{-a_1 + (-1)^i \sqrt{{a_1}^2 + {a_2}^2 - {a_0}^2}}{(a_0 - a_2)}\ i = 1, 2 \tag{6}$$

Formula (6) gives up to two solutions, $\theta_{2,i} = 2\arctan(t_i)$ for $i = 1, 2$, corresponding to the two possible assembly modes that the spherical dyad constituted by links 3 and 4 (Figure 6a) can get when the directions of its endings R-pair axes are assigned. The back substitution of the up to two computed values of θ_2 into Equation (4b) yields the corresponding values of $\mathbf{u}_3$, which, together with the already known $\mathbf{u}_4$, identify the up to two poses of link 4 that solve the direct position analysis.

Equations (4f) and (4g) allow the solution of the inverse position analysis as follows. The known unit vector $\mathbf{u}_3$ ($\mathbf{u}_4$) is introduced into Equation (4f) (into Equation (4g)) together with the expression given by Equation (4a) (by Equation (4c)) of unit vector $\mathbf{u}_2$ (unit vector $\mathbf{u}_5$). The introduction of these known vectors and functions into Equation (4f) (into Equation (4g)) makes it a trigonometric equation in θ_1 (in θ_6), which has the same canonical form of Equation (5), where θ_1 (θ_6) replaces θ_2 and the coefficients have new values that are computable through simple algebraic manipulations. The so-transformed Equation (4f) (Equation (4g)) is solvable in closed form, as it was done for Equation (5), through the half-angle tangent substitution, and it gives up to two values for θ_1 (for θ_6), which are computable by means of a formula formally equal to Equation (6), where the new values of the coefficients have been introduced. With reference to Figure 6a, the so-computed values of θ_1 (of θ_6) correspond to the up to two possible assembly modes that the spherical dyad, constituted by links 2 and 3 (by links 5 and 6), can get when the directions of its ending R-pair axes are assigned. The back substitution of the computed values of θ_6 into Equation (4c) allows for the computation of the corresponding values of unit vector $\mathbf{u}_5$, which, when introduced into Equation (4d), make it possible for the computation of the corresponding values of θ_5 to be conducted through the following formulas:

$$Eq.(4d) \Rightarrow \left\{ \begin{array}{l} \sin\theta_5 = \frac{\mathbf{u}_4\cdot(\mathbf{u}_5\times\mathbf{u}_6)}{(\mathbf{u}_5\times\mathbf{u}_6)\cdot(\mathbf{u}_5\times\mathbf{u}_6)} \\ \cos\theta_5 = \frac{\mathbf{u}_4\cdot[(\mathbf{u}_5\times\mathbf{u}_6)\times\mathbf{u}_5]}{[(\mathbf{u}_5\times\mathbf{u}_6)\times\mathbf{u}_5]\cdot[(\mathbf{u}_5\times\mathbf{u}_6)\times\mathbf{u}_5]} \end{array} \right\rangle \Rightarrow \theta_5 = \mathrm{atan2}\left(\frac{\mathbf{u}_4\cdot(\mathbf{u}_5\times\mathbf{u}_6)}{(\mathbf{u}_5\times\mathbf{u}_6)\cdot(\mathbf{u}_5\times\mathbf{u}_6)}, \frac{\mathbf{u}_4\cdot[(\mathbf{u}_5\times\mathbf{u}_6)\times\mathbf{u}_5]}{[(\mathbf{u}_5\times\mathbf{u}_6)\times\mathbf{u}_5]\cdot[(\mathbf{u}_5\times\mathbf{u}_6)\times\mathbf{u}_5]} \right) \tag{7}$$

Since, for each pose of link 4 (i.e., value of ($\mathbf{u}_3$, $\mathbf{u}_4$)), up to two values of θ_1 and (θ_5, θ_6) are computable, the inverse position analysis admits up to four values of (θ_1, θ_5, θ_6) as solutions, which are all expressible in closed form.

In order to map the *orientation workspace* (OW) of link 4, the two Cartesian references—$Cx_1y_1z_1$, fixed to link 1, and $Cx_4y_4z_4$, fixed to link 4—are introduced as detailed in Figure 13.

With reference to Figure 13, both of these references have their origin at the SMC, and the directions of their coordinate axes are as follows ($\mathbf{i}_r$, $\mathbf{j}_r$, and $\mathbf{k}_r$, for r = 1, 4, are the unit vectors of the coordinate axes x_r, y_r, and z_r, respectively):

$$\mathbf{i}_1 = \frac{\mathbf{u}_1 + \mathbf{u}_6}{\|\mathbf{u}_1 + \mathbf{u}_6\|};\quad \mathbf{j}_1 = \frac{\mathbf{u}_1 \times \mathbf{u}_6}{\|\mathbf{u}_1 \times \mathbf{u}_6\|};\quad \mathbf{k}_1 = \mathbf{i}_1 \times \mathbf{j}_1 = \frac{(\mathbf{u}_1 + \mathbf{u}_6) \times (\mathbf{u}_1 \times \mathbf{u}_6)}{\|\mathbf{u}_1 + \mathbf{u}_6\|\|\mathbf{u}_1 \times \mathbf{u}_6\|}; \tag{8a}$$

$$\mathbf{i}_4 = \frac{\mathbf{u}_3 + \mathbf{u}_4}{\|\mathbf{u}_3 + \mathbf{u}_4\|};\quad \mathbf{j}_4 = \frac{\mathbf{u}_3 \times \mathbf{u}_4}{\|\mathbf{u}_3 \times \mathbf{u}_4\|};\quad \mathbf{k}_4 = \mathbf{i}_4 \times \mathbf{j}_4 = \frac{(\mathbf{u}_3 + \mathbf{u}_4) \times (\mathbf{u}_3 \times \mathbf{u}_4)}{\|\mathbf{u}_3 + \mathbf{u}_4\|\|\mathbf{u}_3 \times \mathbf{u}_4\|}. \tag{8b}$$

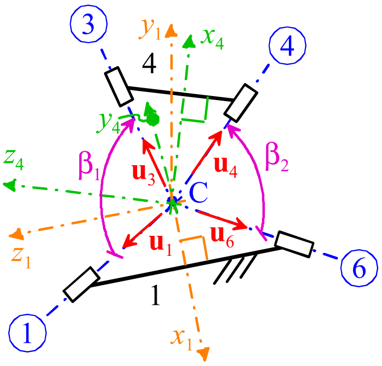

Figure 13. Cartesian reference systems $Cx_1y_1z_1$, fixed to link 1, and $Cx_4y_4z_4$, fixed to link 4.

These notations lead to the writing of the rotation matrix, ${}^1\mathbf{R}_4$, that identifies the orientation of $Cx_4y_4z_4$ (i.e., link 4) with respect to $Cx_1y_1z_1$ (i.e., link 1), as follows:

$$ {}^1\mathbf{R}_4 = [\mathbf{i}_4\ \mathbf{j}_4\ \mathbf{k}_4] \tag{9}$$

where all of the unit vectors, $\mathbf{i}_4$, $\mathbf{j}_4$, and $\mathbf{k}_4$, are measured in $Cx_1y_1z_1$.

Let β_1 and β_2 be the angles between the two joint axes 1 and 3 and between the two joint axes 6 and 4 (see Figure 13), respectively. Both of these angles can range from 0° to 120° because their sides are the ending R-pair axes of the two spherical dyads that simultaneously join link 4 to link 1. Therefore, the OW of link 4 is definable as the set of all of the values of rotation matrix ${}^1\mathbf{R}_4$ that identify link 4 orientations, for which β_1, $\beta_2 \in [0°, 120°]$, that is, the following formula holds:

$$ \mathrm{OW} \equiv \left\{ {}^1\mathbf{R}_4 \,\middle|\, 0° \le \beta_1, \beta_2 \le 120° \right\} \tag{10}$$

If the angles φ_1, φ_2, and φ_3 are the Cardan angles of the ZYX convention, the rotation matrix ${}^1\mathbf{R}_4$ is explicitly expressible through the following formula:

$$ {}^1\mathbf{R}_4 = \begin{bmatrix} \cos\varphi_1\cos\varphi_2 & \cos\varphi_1\sin\varphi_2\sin\varphi_3 - \sin\varphi_1\cos\varphi_3 & \cos\varphi_1\sin\varphi_2\cos\varphi_3 + \sin]\varphi_1\sin\varphi_3 \\ \sin\varphi_1\cos\varphi_2 & \sin\varphi_1\sin\varphi_2\sin\varphi_3 + \cos\varphi_1\cos\varphi_3 & \sin\varphi_1\sin\varphi_2\cos\varphi_3 - \cos\varphi_1\sin\varphi_3 \\ -\sin\varphi_2 & \cos\varphi_2\sin\varphi_3 & \cos\varphi_2\cos]\varphi_3 \end{bmatrix} \tag{11}$$

which, when compared with Equation (9), yields

$$ \begin{cases} \mathbf{i}_4 = \mathbf{i}_1\cos\varphi_1\cos\varphi_2 + \mathbf{j}_1\sin\varphi_1\cos\varphi_2 - \mathbf{k}_1\sin\varphi_2 \\ \mathbf{j}_4 = \mathbf{i}_1(\cos\varphi_1\sin\varphi_2\sin\varphi_3 - \sin\varphi_1\cos\varphi_3) + \mathbf{j}_1(\sin\varphi_1\sin\varphi_2\sin\varphi_3 + \cos\varphi_1\cos\varphi_3) + \mathbf{k}_1\cos\varphi_2\sin\varphi_3 \\ \mathbf{k}_4 = \mathbf{i}_1(\cos\varphi_1\sin\varphi_2\cos\varphi_3 + \sin\varphi_1\sin\varphi_3) + \mathbf{j}_1(\sin\varphi_1\sin\varphi_2\cos\varphi_3 - \cos\varphi_1\sin\varphi_3) + \mathbf{k}_1\cos\varphi_2\cos\varphi_3 \end{cases} \tag{12}$$

Moreover, Equation (8b) and Figure 13 lead to the following relationships:

$$ \mathbf{u}_1 = \mathbf{i}_1\cos 30° + \mathbf{k}_1\sin 30°;\quad \mathbf{u}_6 = \mathbf{i}_1\cos 30° - \mathbf{k}_1\sin 30°; \tag{13a}$$

$$ \mathbf{u}_3 = \mathbf{i}_4\cos 30° + \mathbf{k}_4\sin 30°;\quad \mathbf{u}_4 = \mathbf{i}_4\cos 30° - \mathbf{k}_4\sin 30° : \tag{13b}$$

$$ \cos\beta_1 = \mathbf{u}_1\cdot\mathbf{u}_3;\quad \cos\beta_2 = \mathbf{u}_6\cdot\mathbf{u}_4. \tag{13c}$$

The introduction of Formulas (12) into Equation (13b) and of the resulting Formulas (13a) and (13b) into Equation (13c) yields

$$ \cos\beta_1 = \cos 30°[\cos\varphi_1\cos\varphi_2\cos 30° + (\cos\varphi_1\sin\varphi_2\cos\varphi_3 + \sin\varphi_1\sin\varphi_3)\sin 30°] + \sin 30°(\cos\varphi_2\cos\varphi_3\sin 30° - \sin\varphi_2\cos 30°) \tag{14a}$$

$$\cos\beta_2 = \cos 30^\circ[\cos\varphi_1\cos\varphi_2\cos 30^\circ - (\cos\varphi_1\sin\varphi_2\cos\varphi_3 + \sin\varphi_1\sin\varphi_3)\sin 30^\circ] + \sin 30^\circ(\sin\varphi_2\cos 30^\circ + \cos\varphi_2\cos\varphi_3\sin 30^\circ) \tag{14b}$$

which make it possible to analytically represent the OW as the solution of the following inequality system:

$$\begin{cases} \cos\beta_1 = f_1(\varphi_1, \varphi_2, \varphi_3) \geq \cos 120^\circ = -0.5 \\ \cos\beta_2 = f_2(\varphi_1, \varphi_2, \varphi_3) \geq \cos 120^\circ = -0.5 \end{cases} \tag{15}$$

where $f_1(\varphi_1, \varphi_2, \varphi_3)$ and $f_2(\varphi_1, \varphi_2, \varphi_3)$ are the analytic expressions that appear at the right-hand sides of Equations (14a) and (14b), respectively. Figure 14a shows the OW borders, that is, the two surfaces—$f_1(\varphi_1, \varphi_2, \varphi_3) = -0.5$ and $f_2(\varphi_1, \varphi_2, \varphi_3) = -0.5$; furthermore, the blue dots of Figure 14b indicate the regions delimited by these two surfaces, where the inequality system (15) is satisfied. The analysis of Figure 14 highlights that the OW is wide enough for many applications.

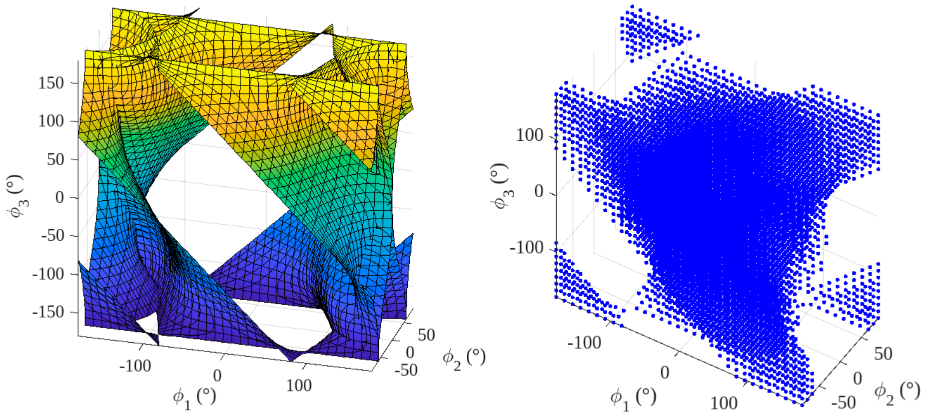

(**a**) (**b**)

Figure 14. Orientation workspace (OW) of a hexagonal SL in the PW mode (φ_1, φ_2, and φ_3 are the Cardan angles of the ZYX convention): (**a**) surfaces delimiting the OW with (**b**) the blue-dotted regions that indicate where inequality system (15) is satisfied.

4. Discussion

The kinematic analyses presented in Section 3 show that both square SLs and hexagonal SLs have position analysis problems that are either trivial or easily solvable in closed form for all of their operation modes. In addition, they have workspaces wide enough for practical applications. With respect to square SLs, which have only single-DOF operation modes, hexagonal SLs, which have two-DOF and three-DOF operation modes, have a wider range of applications, where the switching from two-DOF to three-DOF modes, or vice versa, could be requested. In either case, there are possible applications for all of these SLs. For instance, the switching between the 1st (Figure 3a) and 2nd (Figure 3b) semi-deployed modes of square SLs could be used to obtain a sudden change in flapping direction in a micro/mini robotic insect. Furthermore, the same switching could be used in a multi-functional lid that allows the separate openings of different compartments of a container.

The link/joint collision avoidance and the control of the SL at the transition configurations are two critical issues that must be addressed during their dimensional and detailed designs. Section 3 has presented some technical solutions (Figures 9, 10, and 12) for the link/joint collision avoidance. These solutions are specific to the operation modes that the designer wants to enable, and, at the same time, exclude the possibility of reaching some transition configurations, thus reducing the number of reachable operation modes. For instance, the geometry of Figure 12a,b is compatible only with the PW mode and the left (right) serial mode of the hexagonal SL, and can reach only the transition configuration between these two operation modes and the fully-deployed configuration, which, as explained in Section 2.2, is a transition configuration internal to the PW mode. Other solutions are possible, but, in general, any adopted solution reduces the number of reachable operation modes and modifies the transition graph (Figures 5 and 8) of the particular mechanism geometry that is adopted. In terms of geometric performances, overall sizes of square SLs and of hexagonal SLs at their fully-folded configurations are roughly 1/4 and 1/6, respectively, of those they have at their fully-deployed configurations.

The SL configuration at a transition configuration is controllable by using clutches that either lock/unlock some passive R-pairs, or change the actuated joints, or even just limit the motion of some joints at/or near a transition configuration. The complexity of these systems depends on the specific application. Indeed, if, for instance, the mechanisms are moved directly by an on-site worker, as it may happen in many construction sites, no specific device is necessary. Either way, for all of the studied SLs, the steps necessary for the transition between two operation modes that share a transition configuration can be summarized as follows:

(1) reaching the transition configuration;
(2) locking/forbidding the unwanted local mobility, through the above-mentioned devices, so that only the exit into the wanted operation mode becomes possible;
(3) moving into the wanted operation mode, and then removing the constraints introduced in step (2).

Of course, the transition between two operation modes that do not share a transition configuration and are connected only through a path of the transition graph (Figures 5 and 8) needs the repetition of the above-listed steps in all of the intermediate transitions indicated by the path that joins them.

5. Conclusions

The non-redundant spherical linkages (SL) with architectures coming from regular polygons have been analyzed to identify foldable/deployable architectures. These analyses lead to the conclusion that only those coming from squares or hexagons can be foldable/deployable.

The operation modes and the transition configurations of square SLs and of hexagonal SLs have been identified and related to one another through a graph, named the transition graph. This methodology is novel and is applicable to the analysis of any reconfigurable mechanism.

The kinematic analyses and the workspace determination of square and hexagonal SLs have been presented for each of their operation modes, thus proving that they are suitable for a wide range of applications.

The results of this study are of interest in many applicative fields (field robotics, MEMS/NEMS manufacturing, aerospace, etc.).

Funding: This research was developed at the Laboratory of Mechatronics and Virtual Prototyping (LaMaViP) of Ferrara University (UNIFE), and was funded by FAR2023 UNIFE.

Data Availability Statement: The original contributions presented in this study are included in the article. Further inquiries can be directed to the corresponding author.

Conflicts of Interest: The author declares no conflicts of interest. The funders had no role in the design of the study; in the collection, analyses, or interpretation of data; in the writing of the manuscript; or in the decision to publish the results.

Abbreviations

The following abbreviations are used in this manuscript:

SMC	spherical motion center
DOF	degree of freedom
SL	spherical linkage
CRP	convex regular polygon
OW	orientation workspace
PW	parallel-wrist

References

1. Aimedee, F.; Gogu, G.; Dai, J.S.; Bouzgarrou, C.; Bouton, N. Systematization of morphing in reconfigurable mechanisms. *Mech. Mach. Theory* **2016**, *96 Pt 2*, 215–224. [CrossRef]
2. Wohlhart, K. Kinematotropic linkages. In *Recent Advances in Robot Kinematics*; Lenarcic, J., Parenti-Castelli, V., Eds.; Springer: Dordrecht, The Netherlands, 1996; pp. 359–368. [CrossRef]
3. Galletti, C.; Fanghella, P. Single-loop kinematotropic mechanisms. *Mech. Mach. Theory* **2001**, *36*, 743–761. [CrossRef]
4. Fanghella, P. Stability of branches of a kinematotropic mechanism. In Proceedings of the 2009 ASME/IFToMM International Conference on Reconfigurable Mechanisms and Robots, London, UK, 22–24 June 2009; pp. 41–46, ISBN 978-88-89007-37-2.
5. Kong, X.; Pfurner, M. Type synthesis and reconfiguration analysis of a class of variable-DOF single-loop mechanisms. *Mech. Mach. Theory* **2015**, *85*, 116–128. [CrossRef]
6. Zeng, Q.; Ehmann, K.F.; Cao, J. Design of general kinematotropic mechanisms. *Robot. Comput.-Integr. Manuf.* **2016**, *38*, 67–81. [CrossRef]
7. Wang, J.; Kong, X. A Novel Method for Constructing Multimode Deployable Polyhedron Mechanisms Using Symmetric Spatial Compositional Units. *ASME J. Mech. Robot.* **2019**, *11*, 020907. [CrossRef]
8. López-Custodio, P.C.; Müller, A.; Dai, J.S. A Kinematotropic Parallel Mechanism Reconfiguring Between Three Motion Branches of Different Mobility. In *Advances in Mechanism and Machine Science, Proceedings of the 15th IFToMM World Congress on Mechanism and Machine Science, Krakow, Poland, 30 June–4 July 2019*; Uhl, T., Ed.; Mechanisms and Machine Science; Springer: Cham, Switzerland, 2019; Volume 73, pp. 2611–2620. [CrossRef]
9. López-Custodio, P.C.; Dai, J.S. Design of a Variable-Mobility Linkage Using the Bohemian Dome. *ASME J. Mech. Des.* **2019**, *141*, 092303. [CrossRef]
10. Dai, J.S.; Rees Jones, J. Mobility in Metamorphic Mechanisms of Foldable/Erectable Kinds. *ASME J. Mech. Des.* **1999**, *121*, 375–382. [CrossRef]
11. Zhang, L.; Dai, J.S. Reconfiguration of Spatial Metamorphic Mechanisms. *ASME J. Mech. Robot.* **2009**, *1*, 011012. [CrossRef]
12. Gan, D.; Dai, J.S.; Liao, Q. Mobility Change in Two Types of Metamorphic Parallel Mechanisms. *ASME J. Mech. Robot.* **2009**, *1*, 041007. [CrossRef]
13. Ma, X.; Zhang, K.; Dai, J.S. Novel spherical-planar and Bennett-spherical 6R metamorphic linkages with reconfigurable motion branches. *Mech. Mach. Theory* **2018**, *128*, 628–647. [CrossRef]
14. Jia, G.; Li, B.; Huang, H.; Zhang, D. Type synthesis of metamorphic mechanisms with scissor-like linkage based on different kinds of connecting pairs. *Mech. Mach. Theory* **2020**, *151*, 103848. [CrossRef]
15. Chai, X.; Kang, X.; Gan, D.; Yu, H.; Dai, J.S. Six novel 6R metamorphic mechanisms induced from three-series-connected Bennett linkages that vary among classical linkages. *Mech. Mach. Theory* **2021**, *156*, 104133. [CrossRef]
16. Li, M.; Shi, W.; Chen, J.; Zhuang, Z.; Dai, J.S. Design and Analysis of 8R-Folding Metamorphic Mechanism and Metamorphic Robot. In *Advances in Mechanism and Machine Science, Proceedings of the 16th IFToMM World Congress 2023, Tokyo, Japan, 5–10 November 2023*; Okada, M., Ed.; Mechanisms and Machine Science; Springer: Cham, Switzerland, 2024; Volume 149, pp. 426–435. [CrossRef]
17. Zlatanov, D.; Bonev, I.A.; Gosselin, C.M. Constraint Singularities as C-Space Singularities. In *Advances in Robot Kinematics—Theory and Applications*; Lenarčič, J., Thomas, F., Eds.; Kluwer Academic Publishers: Dordrecht, The Netherlands, 2002; pp. 183–192.
18. Di Gregorio, R. Determination of Singularities in Delta-Like Manipulators. *Int. J. Robot. Res.* **2004**, *23*, 89–96. [CrossRef]
19. Kong, X.; Gosselin, C.M.; Richard, P. Type Synthesis of Parallel Mechanisms with Multiple Operation Modes. *ASME J. Mech. Des.* **2007**, *129*, 595–601. [CrossRef]
20. Kong, X. Reconfiguration Analysis of Multimode Single-Loop Spatial Mechanisms Using Dual Quaternions. *ASME J. Mech. Robot.* **2017**, *9*, 051002. [CrossRef]
21. Lang, R.J. *Origami Design Secrets: Mathematical Methods for an Ancient Art*, 2nd ed.; CRC Press: Boca Raton, FL, USA, 2012; ISBN 978-1-4398-6774-7.

22. Chen, Y. Design of Structural Mechanisms. Ph.D. Thesis, University of Oxford, Oxford, UK, 2003.
23. Demaine, E.D.; O'Rourke, J. *Geometric Folding Algorithms: Linkages, Origami, Polyhedra*; Cambridge University Press: Cambridge, UK, 2007; ISBN 9780511735172.
24. Deng, Z.; Huang, H.; Li, B.; Liu, R. Synthesis of Deployable/Foldable Single Loop Mechanisms with Revolute Joints. *ASME J. Mech. Robot.* **2011**, *3*, 031006. [CrossRef]
25. Angeles, J. *Rational Kinematics*; Springer: New York, NY, USA, 1988; ISBN 978-0-387-96813-1.
26. Ardema, M.D. *Newton-Euler Dynamics*; Springer: New York, NY, USA, 2005; ISBN 978-0-387-23276-8.
27. Hunt, K. *Kinematic Geometry of Mechanisms*; Oxford University Press: New York, NY, USA, 1978; ISBN 9780198562337.
28. Lee, E.A.; Seshia, S.A. *Introduction to Embedded Systems—A Cyber-Physical Systems Approach*, 2nd ed.; MIT Press: Boston, MA, USA, 2017; ISBN 978-0-262-53381-2.
29. Simas, H.; Di Gregorio, R.; Simoni, R.; Gatti, M. Parallel Pointing Systems Suitable for Robotic Total Stations: Selection, Dimensional Synthesis, and Accuracy Analysis. *Machines* **2024**, *12*, 54. [CrossRef]